

1  
2 Investigating the Impact of Saharan Dust Aerosols on Analyses and Forecasts of African  
3 Easterly Waves by Constraining Aerosol Effects in Radiance Data Assimilation  
4  
5  
6  
7

8 By

9 Dustin F. P. Grogan<sup>1</sup>

10 Cheng-Hsuan Lu<sup>1,2</sup>

11 Shih-Wei Wei<sup>1,2</sup>

12 Sheng-Po Chen<sup>1,3</sup>

- 13  
14 1. University at Albany, State University of New York, Albany, NY  
15 2. Joint Center for Satellite Data Assimilation, Boulder, CO  
16 3. Department of Chemistry, National Central University, Taoyuan, Taiwan  
17

18  
19 Submitted to

20  
21 Atmospheric Chemistry and Physics  
22

23 on

24  
25 February 15<sup>th</sup>, 2021  
26

27 Revised on

28  
29 January 25<sup>th</sup>, 2022  
30  
31  
32

33 Corresponding author: Dustin Grogan, University at Albany, 1400 Washington Ave, Albany, NY  
34 12222; dgrogan@albany.edu

35 **Abstract**

36         This study incorporates aerosol effects into satellite radiance calculations within the  
37 Global Data Assimilation System (GDAS) to investigate its impact on the analyses and forecasts  
38 of African easterly waves (AEWs). Analysis fields from the aerosol-aware assimilation  
39 experiment were compared to an aerosol-blind control during August 2017. The results showed  
40 that the aerosol-aware assimilation warmed the Saharan boundary layer, accelerated the African  
41 easterly jet, and modified the time-averaged AEWs by enhancing the northern track and reducing  
42 the southern track. The changes to the tracks are qualitatively consistent with arguments of  
43 baroclinic and barotropic instability. During the time period, we also examined two AEWs that  
44 developed Hurricanes Gert and Harvey over the Atlantic, but were structurally different over  
45 Africa; the AEW for Gert consisted of a southern vortex, while the AEW for Harvey consisted of  
46 a northern and southern vortex. Analysis differences of the cases showed stronger vorticity  
47 changes for the AEW that developed Harvey, which we attribute to the aerosol-aware  
48 assimilation capturing the radiative effects of a large-scale Saharan dust plume interacting with  
49 the northern vortex of the wave. Subsequent forecasts for the AEW cases using the Global  
50 Forecast System (GFS, v14) showed that the aerosol-aware assimilation reduced errors in the  
51 downstream vorticity structure for the AEW that developed Harvey; neutral improvement was  
52 found for the AEW that develop Gert. Thus, aerosol-affected radiances in the assimilation  
53 system have the ability to account for dust radiative effects on the analyzed AEWs, which in turn  
54 can improve the forecasting of AEWs downstream.

55

56

57

58

59 **1. Introduction**

60 In regions around the world, aerosols can have a profound impact on weather. This is  
61 especially the case over North Africa as it houses the Saharan Desert, which is the largest emitter  
62 of mineral dust aerosols, and African Easterly Waves (AEWs), which bring crucial rainfall to  
63 populations in the Sahel.

64 AEWs are the dominant synoptic-scale disturbance over North Africa from March to  
65 October (Carlson 1969; Burpee 1972). The waves develop along the African easterly jet (AEJ),  
66 which is a tropospheric jet (~650 hPa) whose axis is centered in the Sahel (~15°N). The AEWs  
67 are also maintained by the AEJ through barotropic and baroclinic energy conversions (Norquist  
68 et al. 1977). Consequently, the AEWs can have two cyclonic circulations (vortices) that reside  
69 on either side of the AEJ axis (Reed et al. 1988; Pytharilous and Thorncroft 1999). The vortex  
70 south of the AEJ peaks at ~650 hPa and is frequently coupled to moist convection (Kiladis et al.  
71 2006; Berry and Thorncroft 2005), while the northern vortex peaks at ~850 hPa, is dry, and can  
72 be immersed in Saharan dust (Knippertz and Todd 2010; Grogan and Thorncroft 2019). Over the  
73 East Atlantic, the two vortices often merge into a single vortex, which can produce a favorable  
74 environment for tropical cyclogenesis (Schwendike and Jones 2010; Ross and Krishnamurti  
75 2007).

76 During summer, Saharan dust emissions are most active over the western Sahel (16°N-  
77 24°N, 0°-15°W) (Cowie et al. 2014), the same region the AEW northern track resides. The  
78 emissions are driven by enhanced surface winds that blow over dry and erodible regions (Tegan  
79 and Fun 1994; Webb and Strong 2011). Once lifted, the dust mixes within the deep Saharan  
80 boundary layer (Cuesta et al. 2009; Knippertz and Todd 2012) and can form plumes that span  
81 thousands of kilometers. The transport of these large-scale dust plumes has been connected to

82 African easterly waves (Westphal et al. 1988; Jones et al. 2003; Knippertz and Todd 2010;  
83 Nathan et al. 2019; Grogan and Thorncroft 2019; Grogan and Nathan 2021). The dust can also be  
84 carried westward over the Atlantic within the Saharan air layer (SAL) (Karyampudi et al. 1999;  
85 Chen et al. 2010), which is an elevated layer of dry air that originates from the Saharan boundary  
86 layer.

87 Dust directly affects the scattering and absorption of incoming and outgoing radiation of  
88 the atmosphere, which produces heating rates that can influence AEWs through two distinct  
89 pathways (Bercos-Hickey et al. 2017). The first pathway is through the background (time-  
90 averaged) dust fields, which produce heating rates that modify the background temperature and  
91 wind fields (i.e., the AEJ), which in turn affects AEW structure and development (Jones et al  
92 2004; Wilcox et al. 2010; Jury and Santiago 2010). The second pathway is through the formation  
93 of large-scale episodic dust plumes, which produces heating rates that correlate with the wind  
94 and temperature of the AEW to directly affect its growth rates, phase speeds, energetics, and  
95 spatial structures (Grogan et al. 2016, 2017, 2019; Nathan et al. 2017).

96 To incorporate the above-mentioned dust radiative effects on AEWs within a numerical  
97 weather prediction (NWP) system, it is important to represent the episodic nature of the aerosols.  
98 These radiative effects have been included into NWP systems through two approaches: (i)  
99 radiatively coupling aerosols in the forecast model, and (ii) incorporating aerosols in satellite  
100 radiance calculations during data assimilation (DA).

101 For the first approach, aerosol attenuation modifies the heating rates within the radiation  
102 schemes of the forecast model of the NWP system. Studies have shown that this improves the  
103 forecast skill of several features in dust-affected regions over North Africa and the East Atlantic,  
104 including sea-level pressure and atmospheric temperature (Perez et al. 2006; Mulcahy et al.

105 2014), AEWs linked to tropical cyclogenesis (Reale et al. 2009; Reale et al. 2011; Chen et al.  
106 2015), and the AEJ (Reale et al. 2014). Major efforts are also ongoing to improve aerosol  
107 prediction models, including the particle's emission and removal processes, assimilating  
108 observations such as aerosol optical depth (AOD), and model verification and evaluation (see  
109 Benedetti et al. (2018) for a comprehensive discussion). Such advances in aerosol prediction  
110 models can, in turn, improve weather prediction. But despite these advances, the radiative  
111 coupling of episodic aerosols in the NWP system is often not feasible in an operational setting  
112 due to computational costs. Thus, most operational NWP systems use prescribed aerosol  
113 climatologies, such as the NCEP operational Global Forecast System (GFS; Hou et al. 2002) and  
114 the ECMWF integrated forecast system (IFS; Bozzo et al. 2017). Consequently, the NWP system  
115 sacrifices the ability to represent episodic aerosol signals.

116 For the second approach, aerosol transmittance effects are considered during radiance  
117 DA, which modifies the analysis fields of the NWP system. Kim et al. (2018) demonstrated this  
118 approach by including 3-hourly aerosol fields from the Goddard Chemistry Aerosol Radiation  
119 and Transport (GOCART) model into the radiance calculations within the Goddard Earth  
120 Observing System (GEOS)-Atmospheric Data Assimilation System (ADAS). Kim et al. (2018)  
121 showed that when aerosols were considered, they found the fit to observations improved for  
122 satellite infrared (IR) sounders due to accounting for the aerosol transmittance effects in the form  
123 of cooling brightness temperatures (BT), which has been observed in previous studies (e.g.,  
124 Sokolik 2002). As a result, the cooling of BTs led to warmer analyzed surface temperatures in  
125 the Tropical Atlantic. Similarly, Wei et al. (2020, 2021) showed that when including aerosols  
126 from NOAA's Environmental Modeling System (NEMS) GFS Aerosol Component (NGAC) into  
127 NCEP's global data assimilation system (GDAS), the aerosol transmittance effects warmed

128 analyzed sea-surface temperatures and low-level air temperatures over the Atlantic and Africa.  
129 Wei et al. (2020) also showed that the aerosols improved GFS forecasts of vector winds and  
130 geopotential heights at multiple levels in the tropical region.

131 Incorporating aerosol transmittance effects into the radiance calculation of DA is  
132 excluded from all NWP centers, despite its relatively low computation costs and its potential to  
133 leverage aerosol-affected radiances in a physical and consistent way. But more studies  
134 investigating this approach are needed. For example, no study has used this approach to examine  
135 the impacts of dust radiative effects on AEWs in the NWP system. Motivated by the results in  
136 Kim et. al. (2018) and Wei et al. (2020, 2021), along with the physical understanding of dust  
137 radiative effects on AEWs identified above, this study seeks to examine how, and to what extent,  
138 episodic aerosols in the satellite radiance calculations can affect analyses and forecasts of AEWs  
139 over North Africa and the East Atlantic. We focus our analysis on two AEWs during August  
140 2017 that are structurally different over North Africa but later developed hurricanes over the  
141 Atlantic.

142 In Section 2, we describe the model experiments and the methods used to track the  
143 AEWs. Section 3 presents the analyses and forecasts from each experiment and examines the  
144 aerosol-aware experiment in the context of dust radiative effects on AEWs. Section 4 provides  
145 conclusions and a short discussion.

## 146 **2. Experiments and Methods**

### 147 *2.1 Model Experiments*

148 The schematic in Fig. 1 illustrates the workflow of the experiments in this study, which  
149 were conducted from 25 July – 28 August, 2017. The first experiment is an aerosol blind run  
150 (CTL), where aerosols are not considered in the assimilation system. The second experiment is

151 an aerosol-aware run (AER), which constrains aerosol transmittance effects into the radiance  
152 calculations of the assimilation system (i.e., aerosol-affected radiances). For our experiments, we  
153 employ version 14 of the National Centers for Environmental Prediction (NCEP) Global  
154 Forecast System (GFS, v14), which consists of an analysis system, the Global Data Assimilation  
155 System (GDAS), and a forecast model, the global spectral model (GSM), with GFS physics. The  
156 experiments are fully-cycled, which means that each analysis is constructed from their respective  
157 forecasts of the prior cycle.

158         The analyses are constructed using GDAS (Fig. 1: blue), which is a Gridpoint Statistical  
159 Interpolation (GSI) based four-dimensional ensemble-variational (4DEnVar) assimilation  
160 system. The assimilation system is run for 80 ensemble members at T254 (~80km) resolution. In  
161 GDAS, the radiance calculations are conducted by the Community Radiance Transfer Model  
162 (CRTM) (Lu et al. 2021). The CRTM generates simulated brightness temperatures (BT) and  
163 computes the radiance sensitivities with respect to the state variables (Han et al. 2006).

164         For both experiments, various observations are ingested into GDAS, including the  
165 conventional dataset (e.g., radiosondes, ships, buoys, etc.), and satellite observations (e.g.,  
166 retrievals and radiances) (Fig. 1: gray). For the radiance observations, we include the level 1  
167 product of IR and microwave sensors, which are pre-processed by NOAA's National  
168 Environmental Satellite, Data, and Information Service (NESDIS). For a complete list of the  
169 thermal IR sensors, see Table 1 of Wei et al. (2021).

170         For AER, aerosol transmittance effects can be constrained in CRTM by ingesting three-  
171 dimensional aerosol mixing ratios into GDAS. CRTM contains look-up tables for aerosol optical  
172 properties—absorption coefficient, single scattering albedo, and asymmetric factor—to compute

173 the aerosol-affected radiances (Lu et al. 2021). The optical properties are based on the Optical  
174 Properties of Atmospheric Composition (OPAC) software package (Hess et al. 1998).

175 The aerosol mixing ratios are provided by the NEMS GFS Aerosol Component model  
176 (NGAC, v2) (Fig. 1: gold), which is based on GOCART (Colarco et al. 2010). NGAC simulates  
177 the emission, mixing, transport and removal (wet and dry) for 15 externally mixed aerosols,  
178 including dust, sea salt, sulfate, organic carbon, and black carbon. (Lu et al. 2016; Wang et al.,  
179 2018). The NGAC forecasts are used to predict the aerosol mixing ratios during the analysis  
180 window of each cycle. Like the meteorological fields, the aerosol mixing ratios are interpolated  
181 to the observations in space and time using the First Guess at Appropriate Time (FGAT) (Lorenc  
182 and Rawlins 2005). Figure 2 shows the NGAC forecasts total AOD (all aerosols at 550nm)  
183 averaged over 1 – 28 August, 2017. The AOD peaks over the Western Sahara, near the coast of  
184 West Africa, and in the Bodéléle Depression, within the interior of the continent, which are  
185 consistent with source regions over summertime in North Africa (Engelstader and Washington,  
186 2007). The AOD, however, overestimates the hotspots by ~25% when compared to the summer  
187 AOD climatology from the Modern-Era Retrospective analysis for Research and applications  
188 (MERRA, v2) (Randles et al. 2016). Nonetheless, the use of NGAC does not affect our  
189 qualitative interpretation of the aerosol-affected radiances on the analyses and forecasts.

190 We also conducted short-range forecasts in each experiments' fully cycled system. To do  
191 this, the forecast model within GFS runs 120-hr weather forecasts at T670 (~30km) resolution,  
192 which are initialized on 00 UTC of each day (Fig. 1: green). The forecast model does account for  
193 aerosol radiative effects using prescribed monthly aerosol climatologies from OPAC (Hess et al.  
194 1998). But for both experiments, we use the *same* configuration in the forecast model, which



195 means that changes to the forecasts arise solely by the model's response to the analysis  
196 differences, rather than the physics driving the forecast model.

197 To demonstrate the aerosol impact on the IR radiances, Fig. 3 shows a timeseries of each  
198 experiment's observation-minus-forecast (OMF) BT for an IR channel (12.93  $\mu\text{m}$ ) from the  
199 Infrared Atmospheric Sounding Interferometer (IASI); the channel and sensor are representative  
200 for other IR window channels and thermal IR sensors, respectively. For both experiments, Fig. 3  
201 shows that the OMFs, which are averaged over North Africa and the East Atlantic, have a similar  
202 root-mean-square (RMS) (top) and negative, or cold, bias (bottom) during the period of interest.  
203 But for the cold bias, the AER run (red) is slightly more positive than the CTL run (blue). This  
204 reduction in the cold bias for AER is due to the incorporation of aerosol transmittance effects on  
205 the forecast (simulated) BT (via scattering). The average impacts are small ( $\sim 1.7$  K) over the  
206 region, but the bias differences can be substantial (up to  $\sim 10$  K) in localized regions during  
207 strong Saharan dust events (Sokolik et al. 2001). When the aerosol-affected OMFs are  
208 assimilated, this produces warmer analyzed temperatures at low-levels in the atmosphere  
209 (Weaver et al. 2003; Kim et al. 2018; Wei et al. 2021).

## 210 *2.2 Wave tracking*

211 To identify the synoptic wave patterns during the period of interest, we used an objective  
212 tracking algorithm similar to that in Brammer and Thorncroft (2015). Briefly, the tracking  
213 algorithm involves analyzing mass-weighted centers of vorticity at multiple levels (i.e., curvature  
214 vorticity at 850, 700, and 500 hPa; relative vorticity at 850 and 700 hPa). The wave center is then  
215 determined from a weighted average of the centers within a specified radius (500 km). For each  
216 experiment, the wave centers were extracted using the 6-hourly analysis fields, which identified  
217 several systems that traversed North Africa and the East Atlantic. The tracking included waves

218 that later developed hurricanes, which we focus on in this study given their long lifetimes and  
219 downstream implications.

220 For the time period of interest, two hurricanes developed from AEWs: Gert and Harvey.  
221 Figure 4 shows the objective track locations for the AEWs that developed Hurricanes Gert and  
222 Harvey in the CTL run over North Africa and the East Atlantic. For Gert (solid line), the storm  
223 originates over Northeast Africa, at  $5 - 10^{\circ}\text{N}$ , on the 31<sup>st</sup> of July and moves northwestward over  
224 North Africa before reaching the East Atlantic on the 4<sup>th</sup> of August. In contrast, Harvey (dotted  
225 line) originates from two vortices over North Africa, at  $25 - 29^{\circ}\text{N}$  and  $8 - 12^{\circ}\text{N}$ , that develop on  
226 the 8<sup>th</sup> of August and merge into one vortex near the coast, on the 12<sup>th</sup> of August; the storm then  
227 moves west/southwest over the East Atlantic. Both waves developed hurricanes while over the  
228 western portion of the Atlantic Ocean.

229 Comparison of the track locations for CTL and AER show little difference in the storm  
230 positions during their evolution (not shown). After the initial development, the track locations  
231 among the two cases are less than 250 km. Given the wavelength of the AEWs span 2000 – 5000  
232 km (Burpee 1974), the aerosol-aware assimilation does not appear to have a significant influence  
233 on the wave tracks. Therefore, we use track locations from CTL when investigating the storm  
234 structures in the analyses and forecasts for both cases.

### 235 **3. Results**

#### 236 *3.1 Analysis Differences: Time-average fields*

237 Before investigating the AEW cases shown in Fig. 4, we first examine the aerosol  
238 impacts on the time-averaged background temperature, background zonal wind, and AEW  
239 meridional wind variances.

240 Figure 5 shows cross-sections of the time-averaged background temperature and zonal  
241 wind for CTL (contours) and the AER – CTL difference (colors) averaged over 1 - 28 August,  
242 2017. Consider first the CTL run. The experiment captures the main summertime circulation  
243 features over the region. For temperatures, the warmest air is positioned near the surface over the  
244 Saharan Desert (Fig 5a: 20°N-30°N). This warming sets up a strong meridional temperature  
245 gradient that extends vertically up to ~650 hPa and horizontally across the Sahel and over the  
246 East Atlantic (Fig. 5b: 30°W-20°E). For the zonal wind, there is a well-defined AEJ at 650 hPa  
247 (Fig. 5c: 15°N) that extends across North Africa and the East Atlantic (Fig. 5d: 20°W – 15°E,  
248 10°N – 15°N) and low-level westerlies (800-1000 hPa) that are associated with the West African  
249 Monsoon (WAM) flow (Fig 5c: 8°N-18°N).

250 The AER – CTL differences in Fig. 5 indicate how the aerosol-affected radiances impact  
251 the time-averaged background fields. For temperature, the aerosol impacts warm the boundary  
252 layer over the Sahara and Sahel by ~0.5 K (reddish colors in Fig. 5a: 10°N – 30°N, 1000 hPa –  
253 650 hPa) and cool the marine boundary layer below the SAL by ~0.5 K (blueish colors in Fig.  
254 5b: 15°N – 25°W, 15°N – 30°N). These temperature changes are qualitatively consistent with  
255 enhanced aerosol heating in the boundary layer over the continent and in the SAL offshore. Over  
256 land, the heating peaks at 800 hPa in the Sahel and the southern Saharan Desert (Fig 5a: 15°N -  
257 25°N). The location of the heating indicates that the aerosol-aware assimilation: (i) increases  
258 lapse rates (or reduces static stability) below the peak heating (1000 – 800 hPa) in the Sahel and  
259 southern Sahara and (ii) enhances the meridional temperature gradient below the AEJ (1000-650  
260 hPa) across the Sahel.

261 The AER – CTL differences in temperature support the changes to the background zonal  
262 wind via adjustments to the thermal wind. For example, along the enhanced meridional

263 temperature gradient, AER accelerates the AEJ by  $\sim 0.5 \text{ m s}^{-1}$  (blueish colors in Fig. 5c:  $10^\circ\text{N} -$   
264  $15^\circ\text{N}$ , 700 – 600 hPa, and Fig. 5d:  $20^\circ\text{E} - 30^\circ\text{W}$ ,  $10^\circ\text{N} - 15^\circ\text{N}$ ), and accelerates the westerly  
265 flow of the WAM by about  $\sim 1.0 \text{ m s}^{-1}$  (reddish colors in Fig. 5c:  $12^\circ\text{N} - 19^\circ\text{N}$ , 1000 – 850 hPa).  
266 Away from these features, the structural changes to the zonal wind are more difficult to interpret.  
267 But inspection of the shear difference plots show that the aerosol-aware assimilation: (i)  
268 increases the vertical shear below the AEJ ( $15^\circ\text{N} - 22^\circ\text{N}$ , 900 – 700 hPa) and (ii) decreases the  
269 horizontal shear on the flanks of the AEJ axis ( $8^\circ\text{N} - 18^\circ\text{N}$ , 800 – 600 hPa) (not shown).

270 Figure 6 shows a vertical cross-section of the time-averaged, 2-6 day filtered meridional  
271 wind variances, which is a proxy used to assess AEW amplitudes (Reed et al. 1988; Pytharilous  
272 and Thorncroft 1999). The filtered meridional wind variances capture the two AEW tracks over  
273 the interior of North Africa (contours show the CTL run). For both experiments, the wave  
274 structures peak at levels consistent with AEWs examined in previous studies (south:  $8^\circ\text{N} - 13^\circ\text{N}$ ,  
275 700 – 600 hPa; north:  $18^\circ\text{N} - 22^\circ\text{N}$ , 950 – 800 hPa). But the AER – CTL differences (colors)  
276 show that for the AER run, the meridional wind variances increase by  $\sim 15\%$  in the northern  
277 vortex and decrease by  $\sim 10\%$  in the southern vortex. Note that the AER run also increases the  
278 wind variances near the AEJ core by  $\sim 25\%$  ( $15^\circ\text{N}$ , 600 hPa), but this increase does not change  
279 the peak location of the southern vortex.

280 The differences in the AEW meridional wind variances shown in Fig. 6 are, in part, due  
281 to changes to the background fields, which can be explained by the local wave energetics  
282 (Norquist et al. 1977; Hseih and Cook 2005; Bercos-Hickey et al. 2020). In absence of diabatic  
283 processes, the AEW's southern structure extracts energy from the background via barotropic  
284 conversions, which are proportional to the horizontal shear of the AEJ, while the northern  
285 structure extracts energy via baroclinic energy conversions, which are inversely proportional to

286 the static stability (Thorncroft and Hoskins 1994; Paradis et al. 1995; Thorncroft 1995). This  
287 means that for AER, the changes to the background zonal wind and temperature (i) reduce wind  
288 variances in the southern vortex via decreased horizontal shear on the equatorward side of the  
289 AEJ (barotropic) and (ii) increase wind variances in the northern vortex via reduced static  
290 stability below the AEJ (baroclinic).

291 The qualitative explanation of how aerosol-affected radiances impact the waves via the  
292 background fields aligns with the first of two pathways in which dust can affect AEWs  
293 mentioned in the introduction. That is, the aerosol-aware assimilation captures dust radiative  
294 effects that operate on the analyzed background temperature, AEJ, and thus the AEW wind  
295 variances. But it is worth mentioning that dust radiative effects are also coupled to the forecast  
296 model (i.e., from the OPAC aerosol climatology), which operate on the analysis fields via the  
297 first-guess meteorological fields. Thus in AER, changes to the time-averaged fields in Figs. 5  
298 and 6 are due to the NGAC aerosols in the assimilation system modifying existing radiative  
299 effects imposed by the OPAC aerosol climatology in the forecast model.

### 300 *3.2 Analysis Differences: AEW cases*

301 In this subsection, we examine the impact of the aerosol-aware assimilation on the AEW  
302 analysis fields for our cases described in Section 2.2.

303 Figure 7 compares the structure of the AEW that developed Gert for CTL and AER. The  
304 AEW crosses Africa and the East Atlantic from 31 July – 4 August. During these times, the wave  
305 remains south of the AEJ and is thus largely away from the dust aerosols. But despite this  
306 separation, the aerosol-aware assimilation affects the evolution of the wave structure (Fig 7a, 7c:  
307 colors surrounding the X's). For example, on the 2<sup>nd</sup> of August the AER run decreases the wave,  
308 which at this stage is an open trough (Fig 7a: blueish colors surrounding the X). The vertical

309 structure also shows that the cyclonic vorticity for AER (red) is ~10% less than for CTL (blue)  
310 from 600 – 800 hPa (Fig. 7b). On the 4<sup>th</sup> of August, the wave intensifies as it moves offshore,  
311 forming a closed streamline circulation (Fig. 7c). But similar to the onshore wave, the aerosol  
312 impacts on the vertical structures continue to reduce the vorticity within the storm center by  
313 ~10% (Fig. 7d).

314 Figure 8 compares the structure of the AEW that developed Harvey for CTL and AER.  
315 The AEW develops as two vortices over East Africa on the 8<sup>th</sup> of August, and travels westward.  
316 On the 9<sup>th</sup> of August, the land-based AEW is broad in structure and covers a large portion of the  
317 continent (Fig. 8a). For AER, there are strong changes within both vortex centers, which include  
318 increases in the vorticity around the northern vortex (reddish colors at 18°N) and decreases in the  
319 southern vortex (blueish colors at 14°N). The vertical structures show that vorticity for the  
320 northern vortex is, on average, ~20 – 35% larger from 600-850 hPa (Fig. 8b: cf. solid blue and  
321 solid red), while the southern vortex is ~20 – 35% smaller from 750-850 hPa (Fig. 8b: cf. dotted  
322 blue and dotted red). On the 12<sup>th</sup> of August, the two vortices merge into a single wave offshore.  
323 Compared to the land-based AEW, the amplitudes of the combined wave are weak and its  
324 vertical structure changes little with height (Fig 8c, 8d). Consequently, the aerosol impacts are  
325 reduced, affecting the vorticity by ~5-15% from 1000-500 hPa (Fig. 8d).

326 Over Africa, the aerosol impacts on the AEWs for Gert and Harvey were consistent with  
327 the time-averaged AEW meridional wind variances in Fig. 6, but the impacts were stronger for  
328 Harvey. The story is different offshore as the impacts remain moderate for Gert but weaken for  
329 Harvey; the latter may be due to the merging of the vortices and the positioning of the aerosols.  
330 Therefore, we focus on the land-based stage of the AEWs and further investigate the aerosol  
331 impacts.

332 To understand how the aerosol-aware assimilation impacts our AEW cases, it is  
333 informative to examine the episodic dust plumes and radiance observations. Figure 9 shows a  
334 snapshot of the NGAC AOD (brown contours) for times when the AEW for (a) Gert and (b)  
335 Harvey are over Africa; the X's mark the position of the vortex centers. Overlaying the AOD are  
336 observations from the IASI sensor at the same time; shown are the AER – CTL differences in the  
337 BT at 12.93 $\mu$ m (circles), the same sensor and channel shown in Fig 3. For Gert, the BT  
338 differences surrounding the wave are negative. This indicates that near the wave center, the BTs  
339 are cooler in the AER run (Fig. 9a), but the values are small (light blue circles). In contrast, for  
340 Harvey, the negative values are largest near the northern vortex (dark blue circles), which is also  
341 immersed in a dust plume with AODs over 1.0 (Fig. 9b).

342 When aerosol-affected radiances are assimilated, warmer analyzed temperatures are  
343 typically produced at low-levels over North Africa and the East Atlantic (Kim et al. 2018; Wei et  
344 al. 2021). For the AEW that developed Gert, the degree of warming over Africa is similar to the  
345 time-averaged AER-CTL background temperatures shown in Figs. 5a and 5b. But for the AEW  
346 that developed Harvey in AER, the temperatures over the wave's northern vortex (18-22°N)  
347 warm as much as 1.5 K at mid-levels, 900-600 hPa, which is double the time-average. The  
348 implications of this additional warming on the AEW vorticity is explained below.

349 Grogan and Thorncroft (2019) showed through energetic arguments that the heating from  
350 an episodic dust signal that interacts with the AEW's northern vortex generates eddy available  
351 potential energy ( $APE \sim T'^2$ ). Previous idealized studies have also shown that dust-induced eddy  
352 APE amplifies the northern structure of AEWs (Grogan et al. 2016, 2019; Nathan et al. 2017;  
353 Bercos-Hickey et al. 2017). For the Harvey case in the AER run, the scenario is the same as in  
354 Grogan and Thorncroft (2019), but the aerosol-affected radiances capture the heating from the

355 dust plume, rather than the forecast model, which in turn drives the amplified vorticity in the  
356 AEW's northern vortex.

357 The impact of the episodic dust plume on the northern vortex for the AEW that  
358 developed Harvey aligns with the second pathway in which dust can affect AEWs mentioned in  
359 the introduction. Thus the combined effects of both pathways may help to explain why the  
360 aerosol impacts for the AEW with Harvey are stronger than the AEW with Gert.

### 361 *3.3 Forecast Differences: AEW cases*

362 To examine the impact of the aerosol-aware assimilation on the forecasts for our AEW  
363 cases, we compare the Root-Mean-Square-Error (RMSE) in vorticity for CTL and AER; the  
364 forecasts were verified against their respective analysis. Table 1 shows the RMSE relative  
365 differences between AER and CTL for the 1000 – 500 hPa vorticity following the AEWs. To  
366 compute the RMSE following the AEW at each forecast time, we use the CTL wave locations  
367 shown in Section 2. For Gert, a 10° latitude by 10° longitude window is centered on the wave.  
368 For Harvey, our window over North Africa has a fixed latitude of 5 – 25°N and a 15° longitude  
369 range that is centered on the two vortices; over the Atlantic Ocean, a 10° latitude by 10°  
370 longitude window is centered on the merged vortex.

371 Table 1 shows the AER run produces neutral improvement in the forecasting of the AEW  
372 that developed Gert, as evidenced by the mixture of red and green values in the RMSE relative  
373 differences. Inspection of the forecasts show that both AER and CTL underestimate the  
374 intensification of the AEW when initialized onshore, on 31 July – 2 August, and overestimate the  
375 intensification when initialized offshore, on the 3<sup>rd</sup> of August. As a result, there were several  
376 instances where the RMSE forecast differences did not produce statistically significant results  
377 (i.e., crossed out values for Gert in Table 1).



378 In contrast to the AEW that developed Gert, Table 1 shows the AER run produces  
379 statistically significant improvement in forecasting the AEW that developed Harvey. The largest  
380 improvements are found for the forecasts initialized on the 10<sup>th</sup> and 11<sup>th</sup> of August, with the  
381 forecast on the 10<sup>th</sup> showing reductions in RMSE for every forecast day (errors reduced by ~15-  
382 49%). For the initialized times that we examine for Harvey (8 – 11 August), both the analyzed  
383 amplitudes and AER – CTL vorticity differences were larger than Gert while onshore (cf. Figs. 6  
384 and 8). Inspection of the forecasts reveal that the CTL run continues to suppress the wave  
385 amplitudes downstream, while the AER run better maintains the intensity of the wave as the two  
386 vortices merge over the East Atlantic and travel downstream.

387 In summary, the forecast error of the 1000-500 hPa averaged vorticity for the AEW that  
388 developed Gert are similar among the two experiments, but dramatically reduced in AER for the  
389 AEW that developed Harvey. This marked improvement with Harvey is likely associated with  
390 the aerosol-aware assimilation capturing radiative effects of the large-scale Saharan dust plume  
391 that interacted with the AEWs northern vortex. Therefore, ingesting mixing ratios of episodic  
392 aerosols to constrain radiance calculations within the assimilation system can improve  
393 forecasting the evolution of AEWs.

#### 394 **4. Conclusions and Discussion**

395 In this study, we examined how incorporating time-varying aerosols into the assimilation  
396 of satellite radiances affected the analyses and forecasts from GFS v14 and the corresponding  
397 GDAS. In particular, we investigated the impacts of Saharan dust on AEWs and their  
398 environment over North Africa and the East Atlantic during August 2017. To do this, aerosol  
399 forecasts from the NGAC, v2 model were ingested into GDAS and constrained to the radiance  
400 calculations to produce analysis fields (aerosol-aware) that were compared to a control

401 experiment that excluded aerosols (aerosol-blind). The analysis fields from both cases were then  
402 used to forecast two AEW cases during our time period that were structurally different over  
403 Africa, but later developed Hurricanes Gert and Harvey over the Atlantic Ocean.

404 Analysis differences showed that the aerosol-aware assimilation affected several fields  
405 over North Africa and the East Atlantic. For example, the aerosols warmed the Saharan boundary  
406 layer, accelerated the AEJ and the westerlies associated with the WAM, and modified AEW  
407 meridional variances, with amplitudes increasing within the northern vortex and decreasing in  
408 the southern vortex. The changes in the AEW meridional variances were also consistent with the  
409 vorticity changes for the individual AEW cases examined.

410 The impact of the analysis differences on forecasting our AEW cases depended on the  
411 wave structure. For the AEW that developed Gert, which did not have a northern vortex, RMSE  
412 differences showed that the aerosol-aware experiment produced neutral improvement to the  
413 forecasts of the vorticity field tracking the wave over North Africa and the Atlantic. But for the  
414 AEW that developed Harvey, which had a northern vortex, the aerosol-aware experiment  
415 improved the vorticity field in most forecasts. Moreover, the largest reductions in RMSE  
416 occurred when analysis differences in the AEW structures were largest.

417 In exploring the results, we showed qualitatively that the aerosol-aware experiment (via  
418 NGAC aerosols) captured the two pathways involving dust radiative effects on the AEWs, i.e.,  
419 through dust-induced changes to the AEJ and background temperature fields (first pathway), and  
420 through the interaction between the episodic dust plumes and the waves (second pathway). For  
421 example, the aerosol-aware experiment modified the analyzed background temperature and AEJ,  
422 which in turn modified the analyzed time-averaged AEWs that is consistent with barotropic and  
423 baroclinic instability. Additionally, the aerosol-aware assimilation captured the enhanced

424 warming and vorticity associated with the formation of an episodic dust plume interacting with  
425 the northern vortex of the AEW that developed Harvey. The aerosol impact on the AEW that  
426 developed Harvey is similar to dust-coupled AEWs shown in Grogan and Thorncroft (2019). In  
427 contrast, the impact is absent in the AEW the developed Gert because the wave did not have a  
428 northern vortex nor interact with a dust plume.

429         The improvement on forecasting the AEW that developed Harvey suggests the  
430 importance of the aerosol-aware assimilation capturing dust radiative effects on AEWs involving  
431 episodic dust plumes. Although the AEW that developed Gert was influenced by the aerosol  
432 transmittance effects on the time-averaged background fields, this did not improve forecasting of  
433 the storm. Therefore, investigating more cases that do and do not interact with episodic dust  
434 plumes would better determine the utility of our approach for forecasting AEWs. Moreover,  
435 there are known variabilities in AEW activity (Brammer and Thorncroft 2017) and dust source  
436 regions over West Africa (Wagner et al. 2016), and therefore different scenarios of the AEW-  
437 dust plume interaction should be examined. Nonetheless, forecast improvements such as those  
438 shown for the AEW that developed Harvey are encouraging and could be critical for determining  
439 the timing and location of tropical cyclogenesis that originate from developing AEWs.

440         Aerosol radiative effects can be incorporated into the NWP system through the forecast  
441 model and through the assimilation system. Though few studies focus on the assimilation  
442 approach, such as Kim et al. (2018) and Wei et al. (2021), this study has demonstrated the  
443 importance of incorporating time-varying, episodic aerosols into the satellite radiance  
444 calculations to capture dust radiative effects on the analyzed AEWs. More work, however, is  
445 needed to better understand how to optimize the aerosol-aware assimilation, such as adjusting the  
446 bias-correction and quality-control procedures (Wei et al. 2021). Moreover, future work should

447 investigate how much complexity is needed to represent aerosol processes adequately and  
448 accurately, and thus effectively account for aerosol effects within the NWP system.

#### 449 **Data availability**

450 Analyses and forecasts from the AER and CTL runs can be provided upon request to the  
451 first author of the paper.

#### 452 **Author contributions**

453 DG and SL developed the ideas for the study. SW and SC conducted the numerical  
454 experiments. DG, CL, and SW analyzed and interpreted the results. DG prepared the paper. DG,  
455 CL and SW reviewed the paper.

#### 456 **Competing interests**

457 The authors declare that they have no conflicts of interest.

#### 458 **Acknowledgements**

459 The work presented here is supported by NOAA NWS NGGPS R2O (Award number  
460 #NA15NWS468008). The NWS project is a collaborative effort from the University at Albany  
461 (Cheng-Hsuan Lu, Shih-Wei Wei, Sheng-Po Chen, and Dustin Grogan), NCEP/EMC (Robert  
462 Grumbine, Andrew Collard, Jun Wang, Partha Bhattacharjee, Bert Katz, Xu Li), and  
463 NESDIS/STAR (Quanhua Liu, Zhu Tong). The GDAS experiments were conducted at the  
464 University of Wisconsin-Madison Space Science and Engineering Center's Satellite Simulations  
465 and Data Assimilation Studies computer, or S4, cluster.

466 **References**

- 467 Bercos-Hickey, E., Nathan, T.R., and Chen, S.-H.: Saharan dust and the African easterly jet–  
468 African easterly wave system: structure, location and energetics. *Q. J. R. Meteorol. Soc.*,  
469 143, 2797-2808, <https://doi.org/10.1002/qj.3128>, 2017.
- 470 Bercos-Hickey, E., Nathan, T.R., and Chen, S.-H.: On the Relationship between the African  
471 Easterly Jet, Saharan Mineral Dust Aerosols, and West African Precipitation. *J. Clim.*, 143,  
472 3533-3546, <https://doi.org/10.1175/JCLI-D-18-0661.1>, 2020
- 473 Benedetti A., and Coauthors: Status and future of numerical atmospheric aerosol prediction with  
474 a focus on data requirements. *Atmos. Chem. Phys.*, 18, 10615-10643,  
475 <https://doi.org/10.5194/acp-18-10615-2018>, 2018.
- 476 Berry G.J., and Thorncroft C.D.: Case study of an intense African easterly wave. *Mon. Wea. Rev.*  
477 123: 752-766, <https://doi.org/10.1175/MWR2884.1>, 2005
- 478 Brammer, A., and Thorncroft, C.D.: Variability and evolution of African easterly wave structures  
479 and their relationship with tropical cyclogenesis over the eastern Atlantic. *Mon. Wea. Rev.*  
480 143, 4975-4995, <https://doi.org/10.1175/MWR-D-15-0106.1>, 2015.
- 481 Brammar A., and Thorncroft, C.D.: Spatial and temporal variability of the three-dimensional  
482 flow around African easterly waves. *Mon. Wea. Rev.*, 145, 2879-2897,  
483 <https://doi.org/10.1175/MWR-D-16-0454.1>, 2017.
- 484 Bozzo, A., Remy, S., Benedetti, A., Fleming, J., Betchold, P., Rodwell, M.J., and Morcrette, J.-  
485 J.: Implementation of a CAMS-based aerosol climatology in the IFS. ECMWF Technical  
486 Memorandum, 801. Available at: [https://www.ecmwf.int/en/elibrary/17771-radiation-](https://www.ecmwf.int/en/elibrary/17771-radiation-numerical-weather-prediction)  
487 [numerical-weather-prediction](https://www.ecmwf.int/en/elibrary/17771-radiation-numerical-weather-prediction) (last access: 1 Feb 2021), 2017.
- 488 Burpee, R.W.: The origin and structure of easterly waves in the lower troposphere of North  
489 Africa. *J. Atmos. Sci.*, 29, 77-90, [https://doi.org/10.1175/1520-](https://doi.org/10.1175/1520-0469(1972)029<0077:TOASOE>2.0.CO;2)  
490 [0469\(1972\)029<0077:TOASOE>2.0.CO;2](https://doi.org/10.1175/1520-0469(1972)029<0077:TOASOE>2.0.CO;2), 1972.
- 491 Burpee, R.W.: Characteristics of North African Easterly Waves During the Summers of 1968  
492 and 1969. *J. Atmos. Sci.*, 31, 1556-1570, [https://doi.org/10.1175/1520-](https://doi.org/10.1175/1520-0469(1974)031<1556:CONAEW>2.0.CO;2)  
493 [0469\(1974\)031<1556:CONAEW>2.0.CO;2](https://doi.org/10.1175/1520-0469(1974)031<1556:CONAEW>2.0.CO;2), 1974.
- 494 Carlson, T. N.: Some Remarks on African Disturbances and their Progress over the Tropical  
495 Atlantic. *Mon. Wea. Rev.*, 97, No. 10, 716-726, [https://doi.org/10.1175/1520-](https://doi.org/10.1175/1520-0493(1969)097<0716:SROADA>2.3.CO;2)  
496 [0493\(1969\)097<0716:SROADA>2.3.CO;2](https://doi.org/10.1175/1520-0493(1969)097<0716:SROADA>2.3.CO;2), 1969.
- 497 Chen, S.-H., Liu, Y.-C., Nathan, T.R., Davis, C., Torn, R., Sowa N., Cheng, C.-T., and Chen, J.-  
498 P.: Modeling the effects of dust-radiative forcing on the movement of Hurricane Helene  
499 (2006). *Q. J. R. Meteorol. Soc.*, <https://doi.org/10.1002/qj.2542>, 2015.
- 500 Colarco, P., da Silva A., Chin M., Diehl T.: Online simulations of global aerosol distributions in  
501 the NASA GEOS-4 model and comparisons to satellite and ground-based aerosol optical  
502 depth. *J. Geophys. Res.* 115: D14207, <https://doi.org/10.1029/2009JD012820>, 2010
- 503 Cowie, S.M., Knippertz, P., and Marsham, J.H.: A climatology of dust emission events from  
504 northern Africa using long-term surface observations. *Atmos. Chem. Phys.*, 14, 8579-8597,  
505 <https://doi.org/10.5194/acp-14-8579-2014>, 2014.

- 506 Cuesta, J., Marsham J.H., Parker D.H., Flamant C.: Dynamical mechanisms controlling the  
507 vertical redistribution of dust and the thermodynamic structure of the West Saharan  
508 atmospheric boundary layer during summer. *Atmos. Sci. Lett.* 10: 34-42,  
509 <https://doi.org/10.1002/asl.207>, 2009.
- 510 Engelstaedter, S., and Washington R.: Atmospheric controls on the annual cycle of North African  
511 dust. *J. Geophys. Res.-Atmos.* 112: D03103, <https://doi.org/10.1029/2006JD007195>, 2007.
- 512 Grogan, D.F.P., Nathan, T.R., and Chen, S.-H.: Effect of Saharan dust on the linear dynamics of  
513 African easterly waves. *J. Atmos. Sci.* 73, 891-911, <https://doi.org/10.1175/JAS-D-15-0143.1>, 2016.
- 515 Grogan, D.F.P., Nathan, T.R., and Chen, S.-H.: Saharan dust and the nonlinear evolution of the  
516 African easterly jet–African easterly wave system. *J. Atmos. Sci.* 74, 24-47,  
517 <https://doi.org/10.1175/JAS-D-16-0118.1>, 2017.
- 518 Grogan, D.F.P. and Thorncroft, C.D.: The characteristics of African easterly waves coupled to  
519 Saharan mineral dust aerosols. *Q. J. R. Meteorol. Soc.* 2019, 1–17,  
520 <https://doi.org/10.1002/qj.3483>, 2019.
- 521 Grogan, D.F.P., Nathan, T.R., and Chen, S.-H.: Structural Changes in the African Easterly Jet  
522 and Its Role in Mediating the Effects of Saharan Dust on the Linear Dynamics of African  
523 Easterly Waves. *J. Atmos. Sci.* 76, 3359-3365, <https://doi.org/10.1175/JAS-D-19-0104.1>,  
524 2019.
- 525 Grogan, D.F.P. and Nathan, T.R.: Passive versus active transport of Saharan dust aerosol by  
526 African easterly waves. *Geosciences*, 12, 1509, <https://doi.org/10.3390/atmos12111509>,  
527 2021.
- 528 Han, Y., van Deist, P., Liu, Q., Weng, F., Yan, B., Treason, R., and Derber, J.: JCSDA  
529 community radiative transfer model (CRTM): Version 1. NOAA Technical Report  
530 NESDIS 122. Available at  
531 [https://repository.library.noaa.gov/view/noaa/1157/noaa\\_1157\\_DS1.pdf](https://repository.library.noaa.gov/view/noaa/1157/noaa_1157_DS1.pdf) (last access: 1 Feb  
532 2021), 2006.
- 533 Hess, M.P., Koepke, P., and Shult, I.: Optical properties of aerosol and clouds: The software  
534 package OPAC. *Bull. Amer Meteor. Soc.*, 79, 831-844, [https://doi.org/10.1175/1520-0477\(1998\)079<0831:OPOAAC>2.0.CO;2](https://doi.org/10.1175/1520-0477(1998)079<0831:OPOAAC>2.0.CO;2), 1998.
- 536 Hsieh, J.-S., and Cook, K.H.: Generation of African easterly wave disturbances: relationship to  
537 the African easterly jet. *Mon. Wea. Rev.*, 133, 1311-1327,  
538 <https://doi.org/10.1175/MWR2916.1>, 2005.
- 539 Jones, C., Mahowald, N., Luo, C. The role of easterly waves on African desert dust transport. *J.*  
540 *Clim.* 16: 3617-3628, [https://doi.org/10.1175/1520-0442\(2003\)016<3617:TROEWO>2.0.CO;2](https://doi.org/10.1175/1520-0442(2003)016<3617:TROEWO>2.0.CO;2), 2003.
- 542 Jones, C., Mahowald, N., and Luo, C.: Observational evidence of African desert dust  
543 intensification of easterly waves. *Geophys. Res. Lett.*, 31, L17208,  
544 <https://doi.org/10.1029/2004GL020107>, 2004.
- 545 Jury, M.R. and Santiago, M.J.: Composite analysis of dust impacts on African easterly waves in  
546 the Moderate Resolution Imaging Spectrometer era. *J. Geophys. Res.*, 115, D16213,

547 <https://doi.org/10.1029/2009JD013612>, 2010.

548 Karyampudi, V.M., and Coauthors: Validation of the Saharan Dust Plume Conceptual Model  
549 Using Lidar, Meteosat, and ECMWF Data. *Bull. Amer. Meteor. Soc.*, 1045-1076,  
550 [https://doi.org/10.1175/1520-0477\(1999\)080<1045:VOTSDP>2.0.CO;2](https://doi.org/10.1175/1520-0477(1999)080<1045:VOTSDP>2.0.CO;2), 1999.

551 Kiladis, G.N., Thorncroft, C.D., and Hall, N.M.J.: Three-Dimensional Structure and Dynamics  
552 of African Easterly Waves. Part I: observations. *J. Atmos. Sci.* 63, 2212-2230,  
553 <https://doi.org/10.1175/JAS3741.1>, 2006.

554 Kim, J., Akella, S., da Silva, A.M., Todling, R., and McCarty, W.: Preliminary evaluation of  
555 influence of aerosols on the simulation of brightness temperature in NASA's Goddard  
556 Earth Observing System Atmospheric Data Assimilation System. Technical Report Series  
557 on Global Modeling and Data Assimilation, 49. Available at  
558 <https://ntrs.nasa.gov/api/citations/20180001946/downloads/20180001946.pdf> (last access:  
559 1 Feb 2021), 2018.

560 Knippertz P, and Todd, M.C.: The central west Saharan dust hot spot and its relation to African  
561 easterly waves and extratropical disturbances. *Geophys. Res. Lett.* 115,  
562 <https://doi.org/10.1029/2009D012819>, 2010

563 Knippertz, P., and Todd, M.: Mineral dust aerosols over the Sahara: Meteorological controls on  
564 emission and transport and implications for modeling. *Rev. Geophys.*, 50, RG1007,  
565 <https://doi.org/10.1029/2011RG000362>, 2012.

566 Lorenc, A.C., and Rawlins, F.: Why Does 4D-Var Beat 3D-Var? *Q. J. R. Meteorol. Soc.* 2005,  
567 131, 3247–3257, <https://doi.org/10.1256/qj.05.85>, 2005.

568 Lu, C.-H., and Coauthors: The implementation of NEMS GFS Aerosol Component (NGAC)  
569 Version 1.0 for global dust forecasting at NOAA/NCEP. *Geosci. Model Dev.*, 9, 1906-  
570 1919, <https://doi.org/10.5194/gmd-9-1905-2016>, 2016.

571 Lu, C.-H., and Coauthors: The Aerosol Module in the Community Radiative Transfer Model  
572 (v2.2 and v2.3): accounting for aerosol transmittance effects on the radiance observation  
573 operator, et al. *Geosci. Model Dev.*, under review, <https://doi.org/10.5194/gmd-2021-145>,  
574 2021.

575 Hou, Y.-T., Moorhi, S., and Campana, K.: Parameterization of solar radiation transfer in the  
576 NCEP models. NCEP Office Note 441. Available at  
577 [https://repository.library.noaa.gov/view/noaa/23085/noaa\\_23085\\_DS1.pdf](https://repository.library.noaa.gov/view/noaa/23085/noaa_23085_DS1.pdf) (last access: 1  
578 Feb 2021), 2002.

579 Mulcahey, J.-P., Walters, D.N., Bellouin, N., and Milton, S.F.: Impacts of increasing the aerosol  
580 complexity in the Met Office global numerical weather prediction model. *Atmos. Chem.*  
581 *Phys.*, 14, 4749–4778, <https://doi.org/10.5194/acp-14-4749-2014>, 2014.

582 Nathan, T.R., Grogan, D.F.P., and Chen, S.-H.: Subcritical destabilization of African easterly  
583 waves by Saharan mineral dust. *J. Atmos. Sci.* 74, 1039-1055, [https://doi.org/10.1175/JAS-](https://doi.org/10.1175/JAS-D-16-0247.1)  
584 [D-16-0247.1](https://doi.org/10.1175/JAS-D-16-0247.1), 2017.

585 Nathan, T.R., Grogan, D.F.P. and Chen, S.-H.: Saharan dust transport during the incipient  
586 growth phase of African easterly waves. *Geosciences*, 9, 388,  
587 <https://doi.org/10.3390/geosciences9090388>, 2019.

588 Norquist, D.C., Recker, E.R., and Reed, R.J.: The Energetics of African Wave Disturbances as  
589 observed During Phase III of GATE. *Mon. Wea. Rev.*, 105, 334–342,  
590 [https://doi.org/10.1175/1520-0493\(1977\)105<0334:TEOAWD>2.0.CO;2](https://doi.org/10.1175/1520-0493(1977)105<0334:TEOAWD>2.0.CO;2), 1977.

591 Paradis, D., Lafore, J.-P., Redelsperger, J.-L., and Balaji, V.: African easterly waves and  
592 convection. Part I: linear simulations. *J. Atmos. Sci.*, 52, 1657–1679,  
593 [https://doi.org/10.1175/1520-0469\(1995\)052<1657:AEWACP>2.0.CO;2](https://doi.org/10.1175/1520-0469(1995)052<1657:AEWACP>2.0.CO;2), 1995.

594 Pérez, C., Nickovic, S., Pejanovic, G., Baldasano, J.M., and Özsoy, E.: Interactive dust-radiation  
595 modeling: A step to improve weather forecasts. *J. Geophys. Res. Lett.*, 111, D16206,  
596 <https://doi.org/10.1029/2005JD006717>, 2006.

597 Pytharoulis, I., and Thorncroft, C.D.: The low-level structure of African easterly waves in 1995.  
598 *Mon. Wea. Rev.*, 127, 2266–2280, [https://doi.org/10.1175/1520-0493\(1999\)127<2266:TLLSOA>2.0.CO;2](https://doi.org/10.1175/1520-0493(1999)127<2266:TLLSOA>2.0.CO;2), 1999.

600 Randles, C. A., and Coauthors: The MERRA-2 Aerosol Assimilation. NASA TM-2016-104606,  
601 Vol. 45, NASA Global Modeling and Assimilation Office, 132 pp,  
602 <https://gmao.gsfc.nasa.gov/pubs/docs/Randles887.pdf>, 2016.

603 Reed, R. J., Klinker, E., and Hollingsworth, A.: The structure and characteristics of African  
604 easterly wave disturbances as determined from the ECMWF operational analysis/forecast  
605 system. *Meteorol. Atmos. Phys.*, 38, 22–33, <https://doi.org/10.1007/BF01029944>, 1988.

606 Reale, O., Lau, K.M., Kim, K.-Y., and Brin, E.: Atlantic Tropical Cyclogenetic Processes during  
607 SOP-3 NAMMA in the GEOS-5 Global Data Assimilation and Forecast System. *J. Atmos.*  
608 *Sci.*, 66, 3563–3578, <https://doi.org/10.1175/2009JAS3123.1>, 2009.

609 Reale, O., and Lau, K.M.: Impact of an interactive aerosol on the African easterly jet in the  
610 NASA GOES-5 global forecasting system. *Wea. Forecasting*, 26, 504–519,  
611 <https://doi.org/10.1175/WAF-D-10-05025.1>, 2011.

612 Reale, O., Lau, K.M., da Silva, A.M., and Matsui, T.: Impact of assimilated and interactive  
613 aerosol on tropical cyclogenesis. *Geophys. Res. Lett.*, 41, 3282–3288,  
614 <https://doi.org/10.1002/2014GL059918>, 2014.

615 Ross, R. S., and Krishnamurti, T.N.: Low-level African easterly wave activity and its relation to  
616 Atlantic tropical cyclogenesis in 2001. *Mon. Wea. Rev.*, 135, 3950–3964,  
617 <https://doi.org/10.1175/2007MWR1996.1>, 2007.

618 Schwendike, J., and Jones, S.C.: Convection in an African Easterly Wave over West Africa and  
619 the eastern Atlantic: A model case study of Helene (2006). *Q. J. R. Meteorol. Soc.*, 135,  
620 364–396, <https://doi.org/10.1002/qj.566>, 2010.

621 Sokolik, I.: The spectral radiative signature of wind-blown mineral dust: Implications for remote  
622 sensing in the thermal IR region. *Geophys. Res. Lett.*, 29, NO. 24, 2154,  
623 <https://doi.org/10.1029/2002GL015910>, 2002.

624 Thorncroft, C.D., and Hoskins, B.J.: An idealized study of African easterly waves. I: Linear  
625 theory. *Q. J. R. Meteorol. Soc.*, 120, 953–982, <https://doi.org/10.1002/qj.49712051809>,  
626 1994.

627 Thorncroft, C.D.: An idealized study of African easterly waves. III: More realistic basic states. *Q.*  
628 *J. Roy. Meteorol. Soc.* 121, 1589–1614, <https://doi.org/10.1002/qj.49712152706>, 1995.



629 Tegen, I., and Fung I.: Modeling of mineral dust in the atmosphere: Sources, transport, and  
630 optical thickness. *J. Geophys. Res.* 99, 22897-22914, <https://doi.org/10.1029/94JD01928>,  
631 1994.

632 Wagner, R., Schepanski, K., Heinold, B., and Tegen, I.: Interannual variability in the Saharan  
633 dust source activation—toward understanding the differences between 2007 and 2008. *J.*  
634 *Geophys Res. -Atmos* 121, 4538–4562, <https://doi.org/10.1002/2015JD024302>, 2017.

635 Wang, J., and Coauthors: The implementation of NEMS GFS Aerosol Component (NGAC)  
636 Version 2.0 for global multispecies forecasting at NOAA/NCEP— Part 1: Model  
637 descriptions, *Geosci. Model Dev.*, 11, 2315–2332, [https://doi.org/10.5194/gmd-11-2315-](https://doi.org/10.5194/gmd-11-2315-2018)  
638 [2018](https://doi.org/10.5194/gmd-11-2315-2018), 2018.

639 Weaver, C.J., Joiner, J., and Ginoux, P.: Mineral aerosol contamination of TIROS Operational  
640 Vertical Sounder (TOVS) temperature and moisture retrievals. *J. Geophys. Res.* 2003, 108,  
641 <https://doi.org/10.1029/2002JD002571>, 2003.

642 Webb, N.P., and Strong, C.L.: Soil erodibility dynamics and its representation for wind erosion  
643 and dust emission models. *Aeolian Res.* 3, 165-179,  
644 <https://doi.org/10.1016/j.aeolia.2011.03.002>, 2011.

645 Westphal, D.L., Toon O.B., and Carlson, T.N.: A case study of mobilization and transport of  
646 Saharan dust. *J. Atmos. Sci.* 45, 2145-2175, [https://doi.org/10.1175/1520-](https://doi.org/10.1175/1520-0469(1988)045<2145:ACSOMA>2.0.CO;2)  
647 [0469\(1988\)045<2145:ACSOMA>2.0.CO;2](https://doi.org/10.1175/1520-0469(1988)045<2145:ACSOMA>2.0.CO;2), 1988.

648 Wei, S.-W., Collard, A., Grumbine, R., Liu, Q., and Lu, C.-H.: Impacts of aerosols on  
649 meteorological assimilation: Aerosol impact on simulated brightness temperature and  
650 analysis fields. *JCSDA Quarterly*, 66, Spring 2020, <https://doi.org/10.25923/4pt1-wx36>,  
651 2020.

652 Wei, S.-W., Lu, C.-H., Liu, Q., Collard, A., Zhu, T., Grogan, D.F.P., Li, X., Wang, J., Grumbine  
653 R., and Bhattacharjee, P.: The impact of aerosols on satellite radiance data assimilation  
654 using NCEP global data assimilation system. *Atmosphere*, 12(4), 432,  
655 <https://doi.org/10.3390/atmos12040432>, 2021.

656 Wilcox, E.M., Lau, K.M., and Kim, K.Y.: A northward shift of the North Atlantic Ocean  
657 Intertropical Convergence Zone in response to summertime Saharan dust outbreaks.  
658 *Geophys. Res. Lett.*, 24, L04804, <https://doi.org/10.1029/2009GL041774>, 2010.

659

660

661

662

663

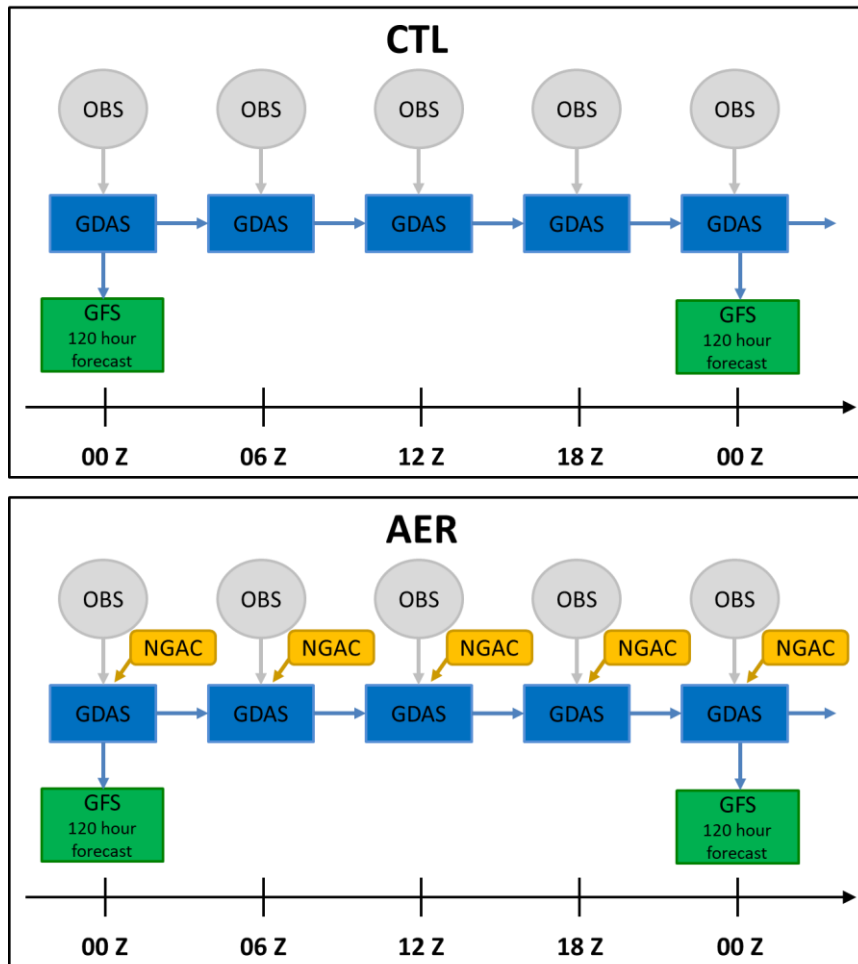
664

665

666

667

668

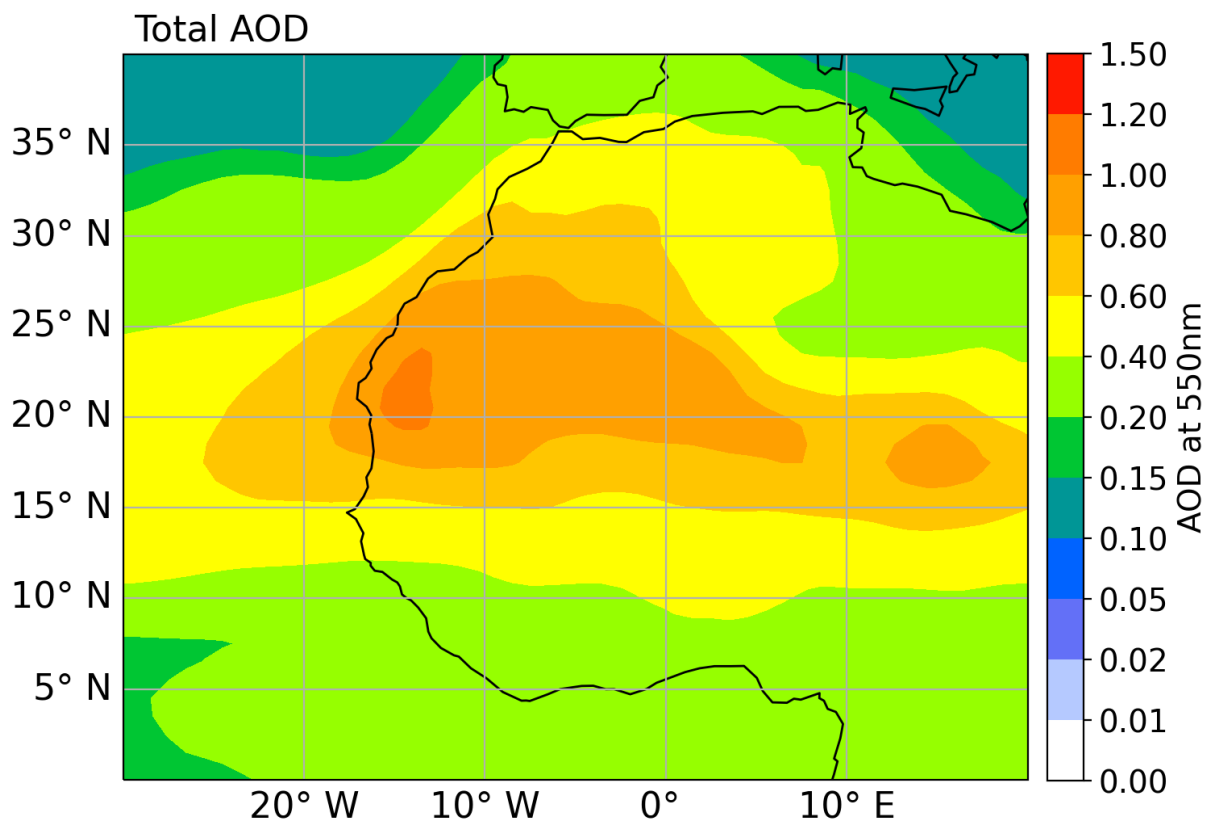


669

670

671 **Figure 1.** Schematic flow chart of the aerosol-blind (CTL) and aerosol-aware (AER) experiments in this study. See text in  
672 section 2.1 for details.

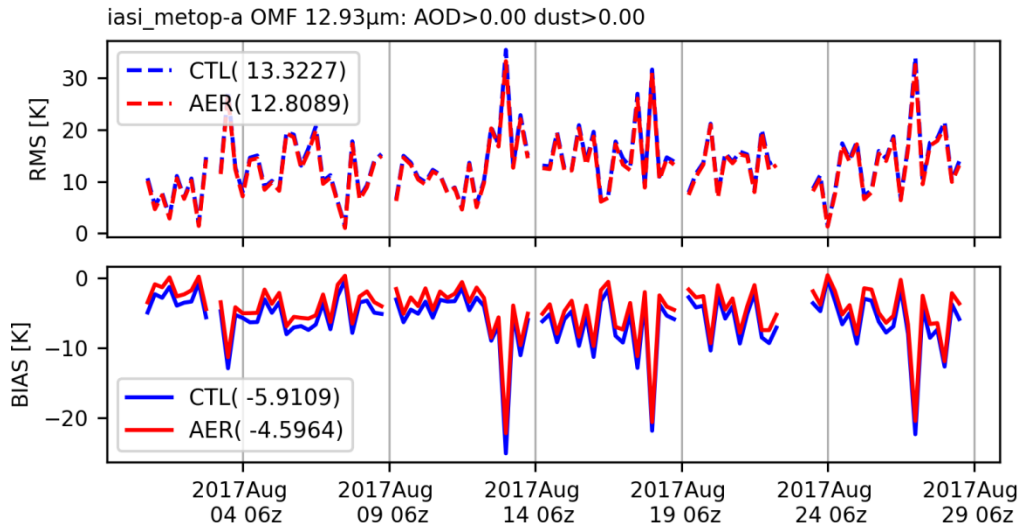
673



674

675 **Figure 2.** Total Aerosol Optical Depth (AOD) from the NGAC forecasts, averaged over 1-28 August, 2017.

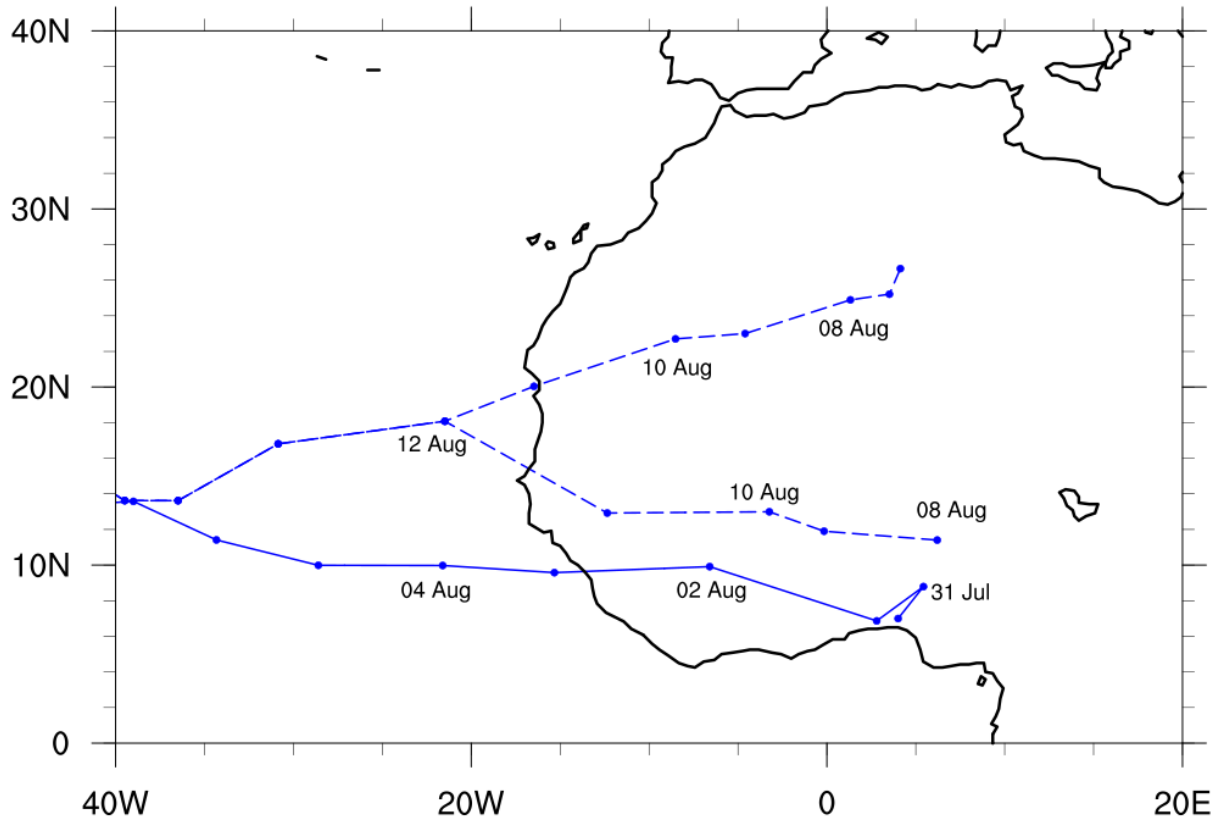
676



677

678  
679  
680  
681  
682

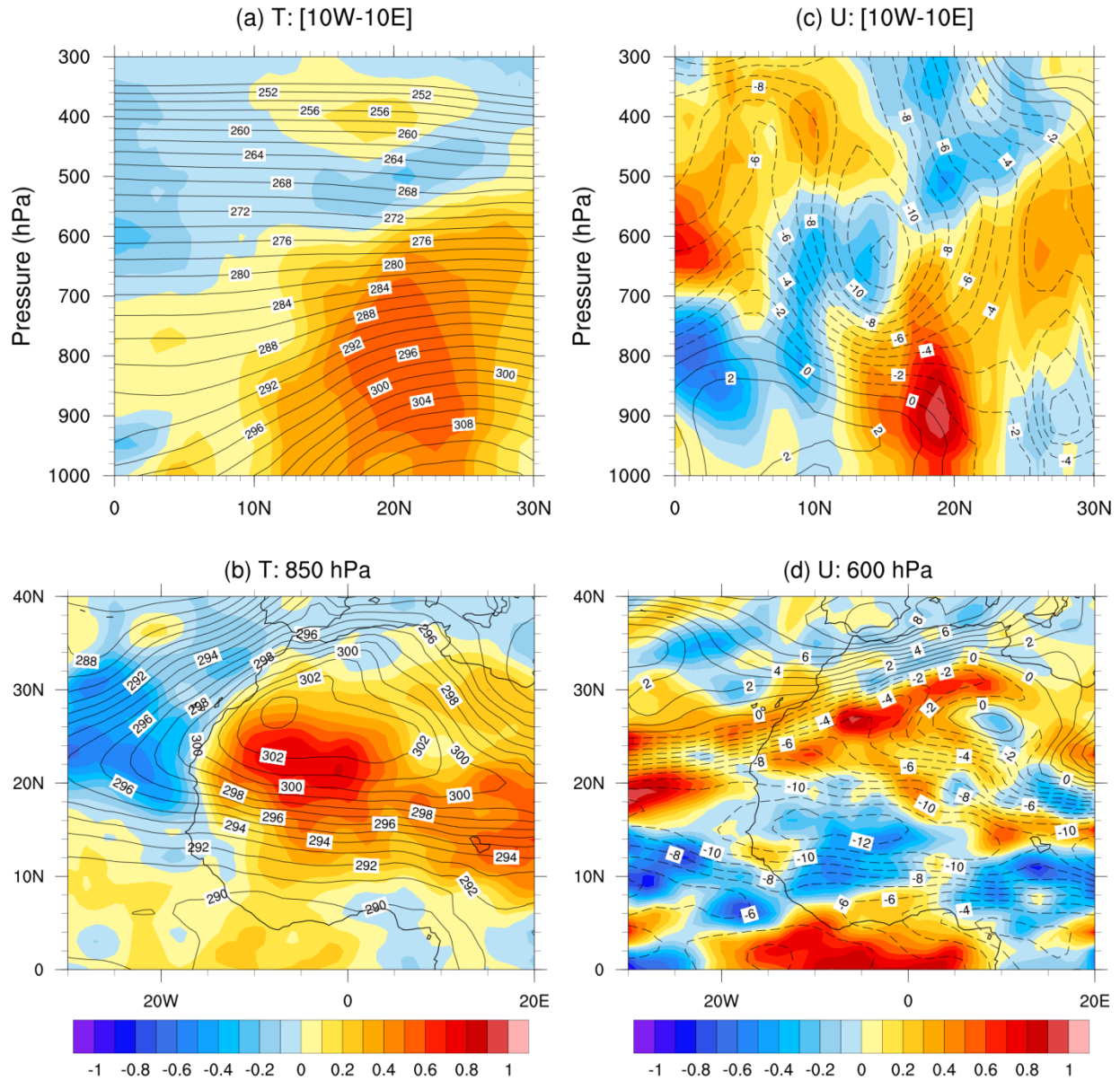
**Figure 3.** Statistics for the observation-minus-forecast (OMF) infrared brightness temperatures (IR BT) ( $12.93\mu\text{m}$ ) from the IASI hyperspectral sensor from CTL (red) and AER (blue). The timeseries includes all observations over the region ( $0\text{-}40^{\circ}\text{N}$ ,  $20^{\circ}\text{E}$ - $30^{\circ}\text{W}$ ), irrespective of aerosol loading. The numbers in the legend are the mean values for the (top) RMS and (bottom) bias for each experiment.



683

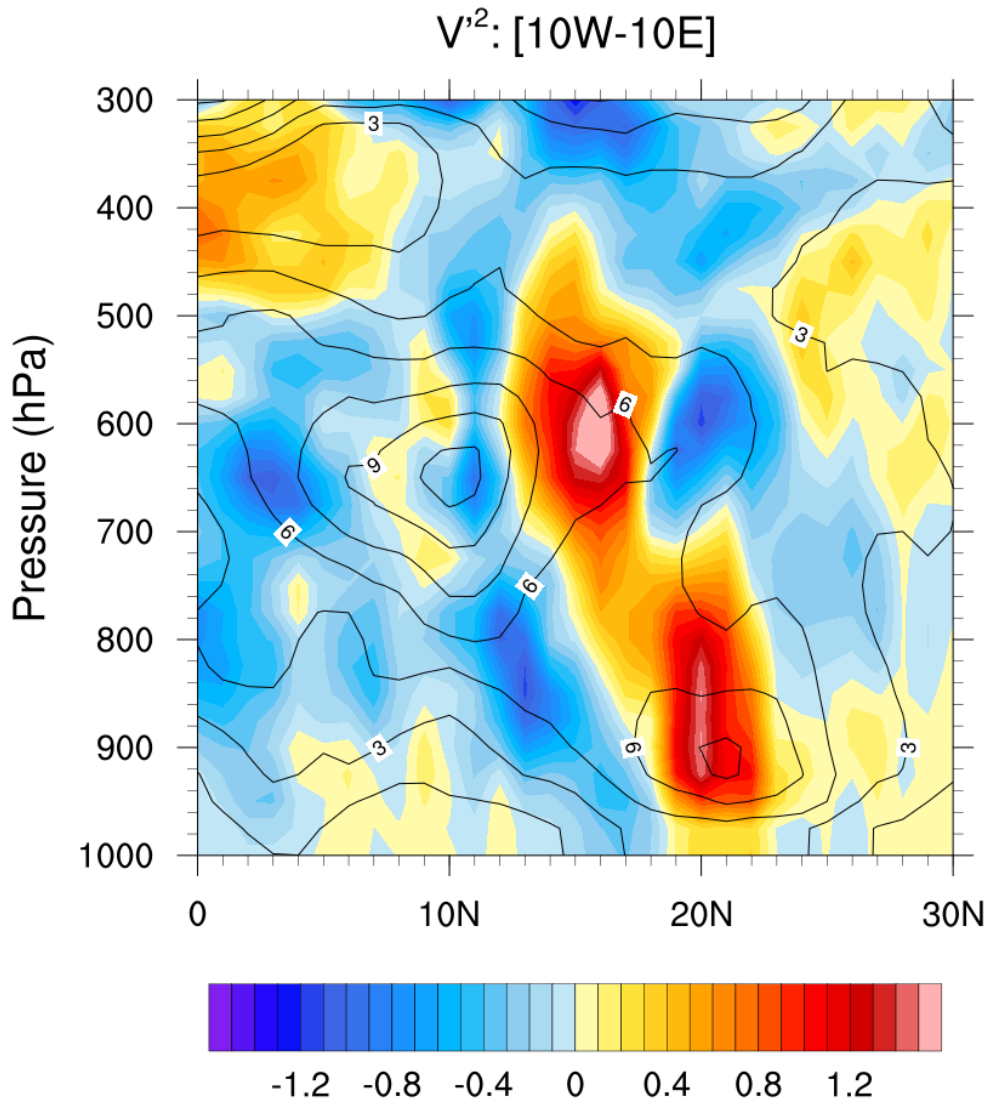
684  
 685  
 686  
 687

**Figure 4.** Daily locations (at 00 UTC) of the AEWs corresponding to Gert (solid) and Harvey (dashed) obtained by the tracking algorithm in the CTL run (time period: August 2017).



688

689 **Figure 5.** Vertical and horizontal cross sections of the CTL analysis (contours) and the AER - CTL analysis difference (colors)  
 690 for (a, b) temperature, T, and (c, d) zonal wind, U. The vertical sections (top) are zonally-averaged from 10°W - 10°E, while  
 691 horizontal sections (bottom) are taken at specified pressure levels. Contour/color units: (a,b) K and (c,d) ms<sup>-1</sup>. The fields are time-  
 692 averaged from 1 - 28 August, 2017.  
 693



694

695 **Figure 6.** Time-averaged 2-6 day filtered meridional wind variances,  $v'^2$ , of the CTL analysis (contours) and the AER – CTL  
 696 analysis difference (colors) zonally-averaged from 10°W – 10°E for August 2017. Contour/color units:  $m^2s^{-2}$ .  
 697

698

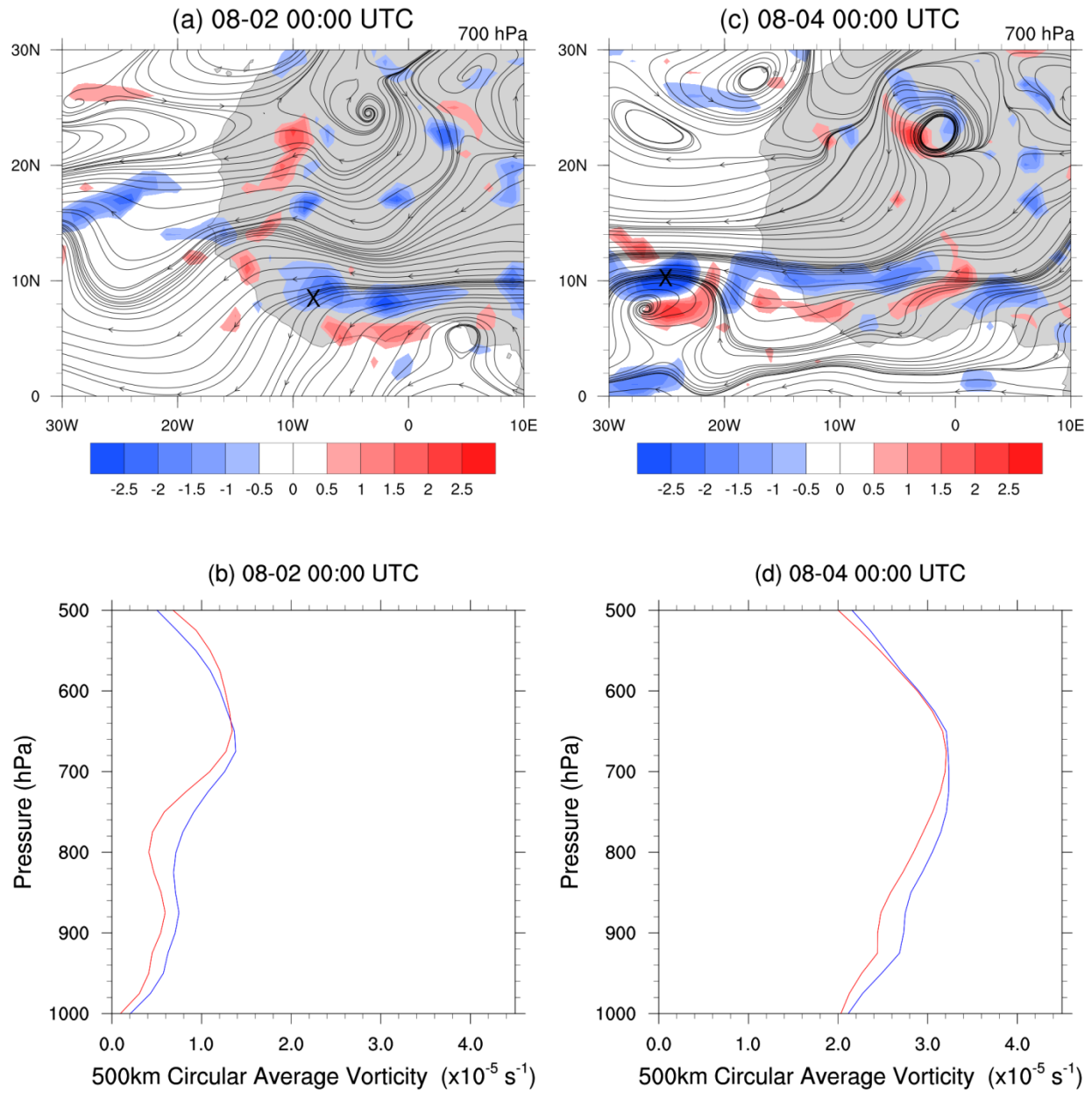
699

700

701

702

703

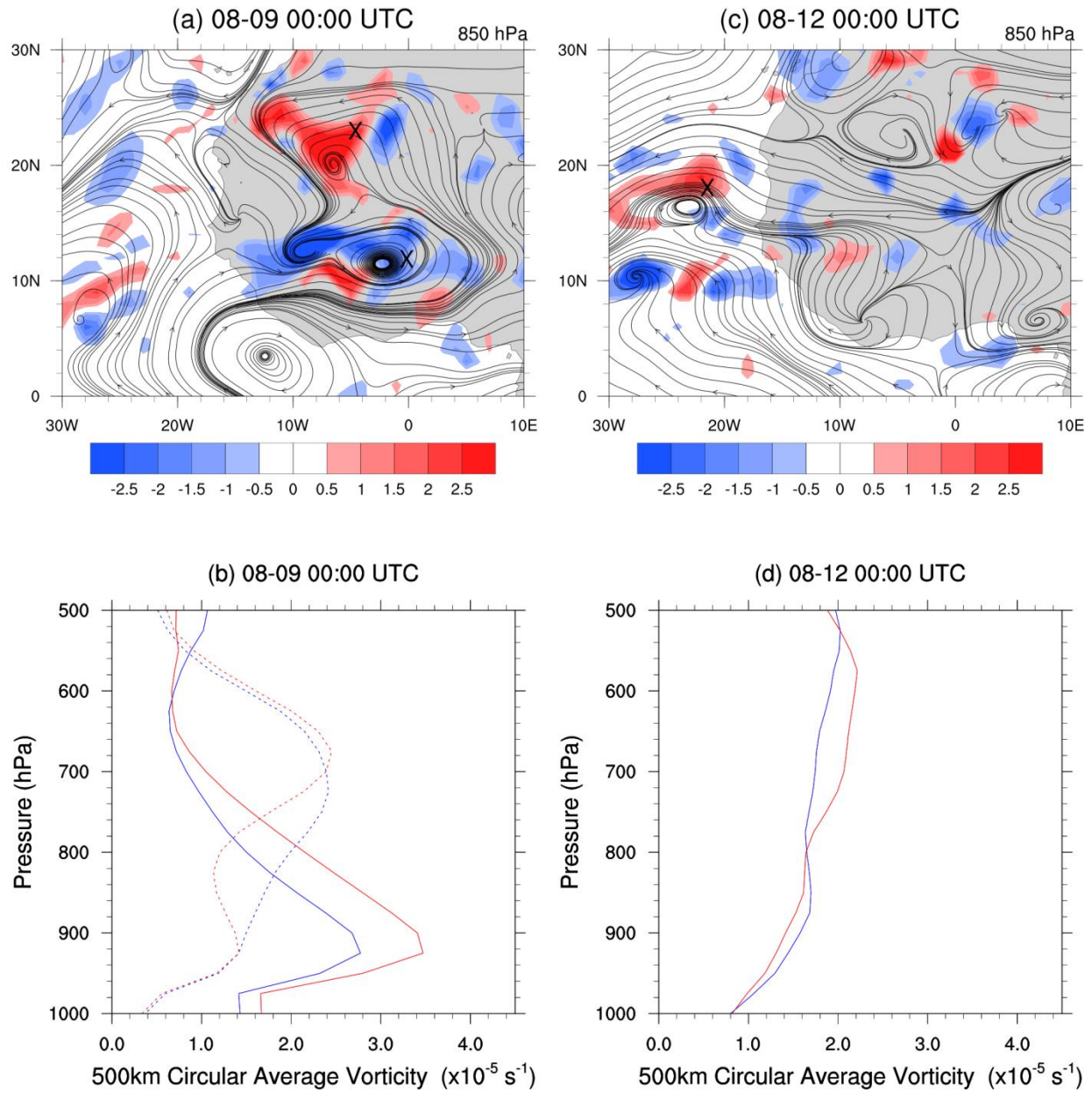


704

705  
706  
707  
708  
709  
710  
711  
712

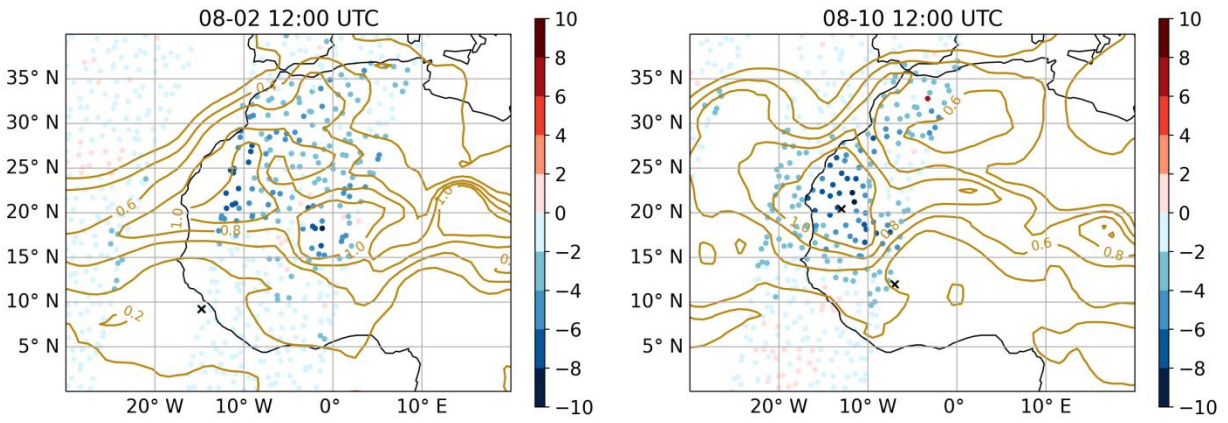
**Figure 7.** The evolution of the AEW associated with Gert on 2<sup>nd</sup> of August (left) and the 4<sup>th</sup> of August (right). The top panels show the 700 hPa CTL streamlines (black) and the AER – CTL 700 hPa cyclonic vorticity differences (red/blue); the ‘X’ marks the wave’s location from the tracking algorithm. The bottom panels show the circular average vorticity (radius 500 km) taken at the X’s for CTL (blue) and AER (red). Note that for the dates in the titles, the first digit corresponds to the month and the second digit to the day.





713  
 714 **Figure 8.** As in Fig. 7, but for the evolution of the AEW associated with Harvey on the 9<sup>th</sup> of August (left) and the 12<sup>th</sup> of August  
 715 (right). The horizontal plots (top) show 850 hPa CTL streamlines and 850 hPa AER-CTL cyclonic vorticity differences, instead of  
 716 700 hPa, to better capture the two-vortex signal. Over Africa (b), we overlay the vertical vorticity structures of the northern  
 717 (solid) and southern (dotted) vortices for CTL (blue) and AER (red).  
 718

719



720

721 **Figure 9.** AER – CTL differences in simulated BT at 12.93 $\mu$ m from the IASI (colored circles) with the NGAC AOD (brown  
 722 contours) on the 2<sup>nd</sup> of August, 12:00 UTC (left) and the 10<sup>th</sup> of August, 12:00 UTC (right). The X's mark the location of the  
 723 wave centers for the AEW that developed Gert (left: 8°N,14°W) and Harvey (right: at 12°N,17°W and 20.5°N,13°W). Colorbar  
 724 units: K.  
 725

726

727

728

729

730

731

732

**Gert**

Initialization	1 day	2 day	3 day	4 day	5 day
31 July	<del>0.13</del>	0.21	0.19	0.38	0.03
1 August	0.17	0.27	0.25	0.10	0.08
2 August	0.19	0.04	0.24	0.10	0.08
3 August	0.06	0.20	0.23	0.09	1.02

**Harvey**

Initialization	1 day	2 day	3 day	4 day	5 day
8 August	0.23	0.05	0.23	0.32	0.27
9 August	0.08	0.07	0.06	0.33	0.32
10 August	0.35	0.32	0.17	0.31	0.49
11 August	0.22	0.39	0.49	0.46	0.64

734  
735  
736  
737  
738  
739

**Table 1.** RMSE relative differences in the 1000 – 500 hPa relative vorticity between the AER and CTL forecasts for the AEWs that developed Gert and Harvey. For each forecast day, the relative differences are calculated by taking (AER-CTL)/CTL of the RMSEs over the region following the AEWs (see text for more details). The green values indicate AER improved the forecast, while red values indicate AER degraded the forecast; crossed-out values were not significant to the 99% confidence interval. The staircase border in each case separates times when the waves are located onshore (upper left) and offshore (lower right).